

Seemingly anisotropic magnetodielectric effect in isotropic EuTiO₃ ceramics

Dalibor Repčák^{1,2,*}, Christelle Kadlec¹, Filip Kadlec¹, Maxim Savinov¹, Martin Kachlák³, Jan Drahokoupil¹, Petr Proschek⁴, Jan Prokleška⁴, Karel Maca^{3,5} and Stanislav Kamba^{1,†}

¹*Institute of Physics, Czech Academy of Sciences, Na Slovance 2, 182 21 Prague 8, Czech Republic*

²*Faculty of Nuclear Sciences and Physical Engineering, Czech Technical University in Prague, Břehová 7, 115 19 Prague 1, Czech Republic*

³*CEITEC-Central European Institute of Technology, Brno University of Technology, Purkyňova 123, 612 00 Brno, Czech Republic*

⁴*Faculty of Mathematics and Physics, Charles University, Ke Karlovu 5, 121 16 Prague 2, Czech Republic*

⁵*Department Of Ceramics and Polymers, Faculty of Mechanical Engineering, Brno University of Technology, Technická 2896/2, 616 69 Brno, Czech Republic*

 (Received 4 May 2020; revised 23 July 2020; accepted 14 September 2020; published 1 October 2020)

In the antiferromagnetic phase of EuTiO₃ ceramics, a seemingly anisotropic magnetodielectric effect (up to 2.5%) was observed via the low-frequency dielectric permittivity measured in external magnetic field below 1.9 T. We explain the effect theoretically by taking into account the demagnetizing field which effectively reduces the internal magnetic flux density by 0.6 T when the external magnetic field is applied perpendicular to the plane of the disk-shaped sample. This finding is also confirmed experimentally by magnetization measurements. The refractive index between 0.2 and 0.5 THz exhibits a large anisotropy in an external magnetic field of up to 7 T. This anisotropy is due to a shift of the ferromagnetic resonance from the microwave to the sub-THz region with external magnetic field applied perpendicular to the magnetic component of the THz radiation. This magnon observation is performed in the strong external magnetic field (above 2 T) and in both paramagnetic and antiferromagnetic phases.

DOI: [10.1103/PhysRevB.102.144402](https://doi.org/10.1103/PhysRevB.102.144402)

I. INTRODUCTION

EuTiO₃ is an incipient ferroelectric antiferromagnet, and since the discovery of these properties by Katsufuji and Takagi [1] in 2001, there have been open questions about the mechanisms underlying its unusual behavior. One of its special features is the anomalously strong spin-phonon coupling which can be detected via the real permittivity ϵ_1 at 1 kHz. This quantity exhibits a 5% decrease upon cooling below the Néel temperature $T_N = 5.5$ K and a 7% increase upon the application of a moderate external magnetic field of 2 T at 2 K. This magnetodielectric effect appears despite the centrosymmetric crystal structure of EuTiO₃ which precludes the linear magnetoelectric coupling. The magnetodielectric effect was shown to be related to a spin pair correlation [1,2] $\langle \mathbf{S}_i \cdot \mathbf{S}_j \rangle$ between the nearest-neighbor sites i and j . The magnetoelectric coupling was explained by a strong third-order E^2H^2 -type spin-lattice coupling [3] for which EuTiO₃ is the subject of ongoing research [4–6].

At room temperature, EuTiO₃ crystallizes in the perovskite structure with the $Pm\bar{3}m$ space group [7]. Upon cooling below 282 K, it undergoes an antiferrodistortive structural phase transition to the tetragonal space group $I4/mcm$ [8–10]. Moreover, each Eu²⁺ ion possesses a fairly large magnetic dipole moment of seven Bohr magnetons, and below T_N , these ions form a G -type antiferromagnetic structure, i.e., all

directly neighboring moments are mutually antiparallel [11,12]. At low temperatures, these moments can be easily oriented even by a weak external magnetic field, so the magnetization achieves its saturation value in a field of approximately 1.0–1.5 T [12,13].

In this paper, we present results of an experimental study of the magnetodielectric effect in EuTiO₃ ceramics depending on the orientation of the external magnetic field. The observed “anisotropy” is revealed to be a consequence of a significant demagnetizing field which arises from the large value of the saturation magnetization and from the weak external magnetic field necessary for the saturation. Furthermore, the complex refractive index $\hat{N} = n + ik$ of EuTiO₃ in the THz region was investigated as a function of the external magnetic field orientation and strength. Its observed strong anisotropy is explained by the magnon dynamics depending on the orientation of the magnetic component of the THz radiation with respect to the external magnetic field.

II. EXPERIMENTAL DETAILS

Bulk polycrystalline ceramic samples were prepared from a powder mixture of Eu₂O₃ (99.995%, specific surface area SSA = 7.55 m²g⁻¹, grain size \approx 100 nm, Verochem) and TiO₂ (99.99% anatase, SSA = 9.75 m²g⁻¹, grain size \approx 200 nm, Verochem). The powder precursors were mixed in a mass ratio calculated from the equation



*Corresponding author: repcek@fzu.cz

†Corresponding author: kamba@fzu.cz

The mixture was homogenized by low-energy ball milling for 48 hours with zirconia balls as milling elements and ethanol as a medium in a polypropylene bottle. The powder was dried and then annealed to react into the EuTiO_3 perovskite phase. The solid-state reaction occurred at a temperature of 1373 K with a dwell time of three hours (heating/cooling rates of 20 K min^{-1}) in a pure hydrogen atmosphere (99.9% purity, pressure of 95 kPa, flow of 51 min^{-1}). The agglomerated powder product was manually homogenized in a mortar. Disk-shaped green bodies were formed by a uniaxial pressure of 10 MPa (diameter $\approx 10 \text{ mm}$; mass $\approx 1 \text{ g}$) followed by cold isostatic pressure of 1000 MPa. Sintering was performed at a temperature of 1673 K with a dwell time of two hours (heating/cooling rates of 10 K min^{-1}) in an inert atmosphere of pure argon (99.999% purity, pressure of 95 kPa, flow of 11 min^{-1}). The relative density (93.2%) of the sintered body together with the open and closed volume porosity (1.4% and 5.4%, respectively) were established by the Archimedes method (EN 623-2) and using the theoretical density of EuTiO_3 ceramics of 6.91 g cm^{-3} . More details about the sample processing are described elsewhere [14].

The purity, crystal structure and texture of the sample were analyzed using x-ray diffraction (automated multipurpose x-ray diffractometer Rigaku SmartLab 3kW; X'Pert PRO PANalytical equipped with Co tube). The sample texture was estimated by calculating the so-called texture index whose values fell between 0.72 and 1.28 for all analyzed x-ray reflections. Details about the texture index determination can be found elsewhere [15]. Thus, the x-ray diffraction analysis has shown single-phase EuTiO_3 ceramics with no texture. An observation of the polished sample surface using an optical microscope revealed an average grain size of about $50 \mu\text{m}$, with the maximum grain size reaching over $100 \mu\text{m}$ [16]. This size of individual grains is sufficiently low, so this ceramic sample can be considered as macroscopically isotropic.

All measurements were performed on the same EuTiO_3 ceramic sample which was consequently postprocessed for each experiment. For experiments in the external magnetic field \mathbf{B} , the field was oriented either parallel with or perpendicular to the incident electric field vector—either that of the low-frequency electric field \mathbf{E}^ω (from 1 Hz to 100 kHz) or to that of the THz radiation.

Low-frequency dielectric measurements were performed using a Novocontrol Alpha-AN high performance impedance analyzer in conjunction with a Janis ST-100 cryostat (5–300 K). Magnetodielectric measurements were performed in a cryomagnet (Cryogenic) at temperatures down to 0.3 K and at magnetic fields up to 15 T. Gold electrodes were deposited on surfaces (with a diameter of $\approx 10 \text{ mm}$) of the sample with a thickness of $\approx 500 \mu\text{m}$. Magnetization in the steady external magnetic field of up to 9 T was measured on a square cuboid sample ($1.5 \times 1.5 \times 5 \text{ mm}$) cut out of the half disk, using a PPMS 9T (Quantum Design) instrument with the vibrating sample magnetometer option.

Low-temperature infrared (IR) reflectivity measurements in the frequency range $30\text{--}670 \text{ cm}^{-1}$ (1–20 THz) were performed using a Bruker IFS-113v Fourier-transform IR spectrometer equipped with a liquid-He-cooled Si bolometer (1.6 K) serving as a detector. Room-temperature mid-IR spectra up to 5000 cm^{-1} were obtained using a pyroelectric

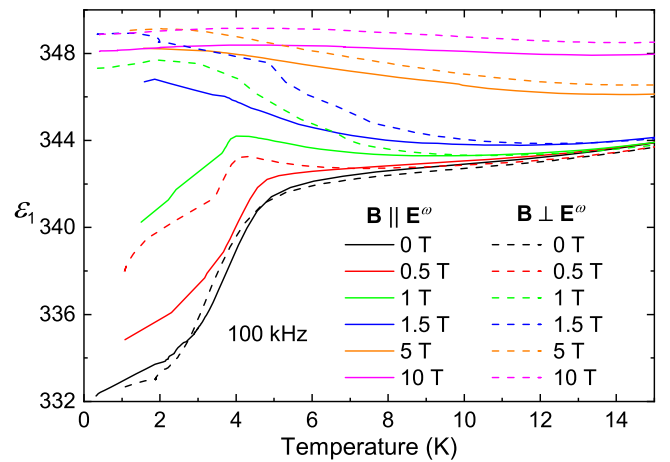


FIG. 1. Temperature dependence of the disk-shaped sample permittivity measured for two orientations of AC (100 kHz) electric field \mathbf{E}^ω with respect to the static external magnetic field \mathbf{B} . \mathbf{E}^ω was always applied perpendicularly to the plane of the half-disk sample whereas \mathbf{B} was pointing either along the sample plane ($\mathbf{B} \perp \mathbf{E}^\omega$) or along the surface normal ($\mathbf{B} \parallel \mathbf{E}^\omega$); see also the inset in Fig. 2.

deuterated triglycine sulfate detector. IR measurements were performed on the polished half-disk shaped sample ($\approx 10 \text{ mm}$ in diameter, about $500 \mu\text{m}$ thick) attached to a 5-mm aperture.

For the low-temperature IR and THz spectroscopies, continuous-He-flow cryostats (Optistat, Oxford Instruments) with polyethylene and mylar windows, respectively, were used. Temperature-dependent THz spectra of complex transmittance between 3 and 35 cm^{-1} were obtained using a custom-made time-domain spectrometer utilizing a Ti:sapphire femtosecond laser. THz spectra with the external magnetic field were measured in a He-bath cryostat with a variable temperature insert (Spectromag, Oxford Instruments) and a superconducting magnet capable of applying external magnetic field up to 7 T. The spectra were recorded in both polarizations in the Voigt geometry, i.e., the electric vector of the THz radiation was parallel with or perpendicular to the external magnetic field, which was applied in the sample plane. The THz measurements were performed on a polished quarter-disk shaped sample (broken half disk, original diameter about 10 mm, thickness $97 \mu\text{m}$) attached to a 5-mm aperture.

III. RESULTS AND DISCUSSION

A. Low-frequency magnetodielectric effect and demagnetizing field

Figure 1 shows the temperature dependence of the real permittivity ε_1 measured at 100 kHz for various values and orientations of the external magnetic field \mathbf{B} . The magnetodielectric effect is clearly observable mainly below $\approx 6 \text{ K}$. The data also indicates that the magnetodielectric effect is present even well above T_N in case of a strong \mathbf{B} . These results are fully consistent with the findings of Katsufuji and Takagi [1]. There is, however, an unexpected discrepancy between the data measured in parallel and perpendicular

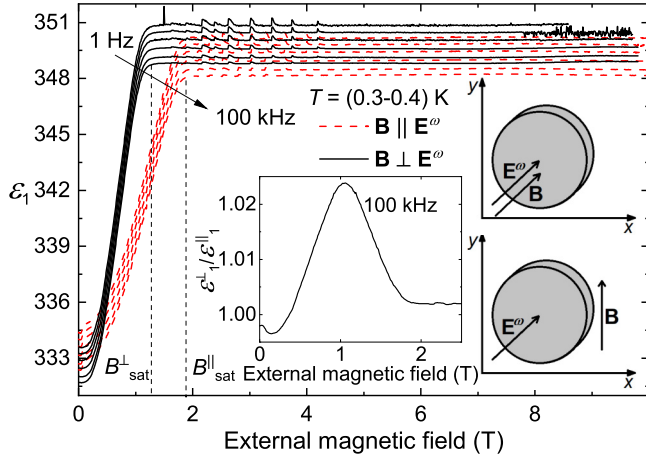


FIG. 2. External magnetic field dependence of the disk-shaped sample permittivity measured for electric field \mathbf{E}^ω (with frequencies 1 Hz, 10 Hz, 100 Hz, 1 kHz, 10 kHz, and 100 kHz) applied perpendicularly to the sample plane, and with the static external magnetic field \mathbf{B} in either of the two orientations ($\mathbf{B} \parallel \mathbf{E}^\omega$ or $\mathbf{B} \perp \mathbf{E}^\omega$, see inset). The temperature was stabilized within 0.3–0.4 K. $B_{\text{sat}}^{\parallel}$ and B_{sat}^{\perp} mark the values of the saturation external magnetic field for both orientations. Inset: Dependence of the ratio ε_1^{\perp} to $\varepsilon_1^{\parallel}$ on external magnetic field for electric field with frequency 100 kHz. ε_1^{\perp} and $\varepsilon_1^{\parallel}$ represent the real permittivity in configuration $\mathbf{B} \perp \mathbf{E}^\omega$ and $\mathbf{B} \parallel \mathbf{E}^\omega$, respectively.

orientations of electric and external magnetic fields. Surprisingly, this “anisotropy” consequently diminishes in the strong external magnetic field.

The influence of the orientation on the real permittivity ε_1 can be seen better from its dependencies on the external magnetic field shown in Fig. 2. Indeed, there is a clearly visible difference (up to $\approx 2.5\%$) between the curves belonging to the orientations $\mathbf{B} \perp \mathbf{E}^\omega$ and $\mathbf{B} \parallel \mathbf{E}^\omega$. This difference vanishes (within the measurement accuracy of a few units) above approximately 1.9 T. The noise present in all curves is caused by weak temperature oscillations. Considering the isotropic character of the sample, the only explanation of the weak anisotropy can be provided by the effect of demagnetizing field.

The demagnetizing field can be expected to be the source of the seeming anisotropy in EuTiO_3 , for two reasons. First, according to the Hund’s rules, Eu^{2+} ions possess a magnetic moment of $7\mu_B$ (Bohr magnetons). Second, these moments are easily orientable by the external magnetic field (the antiferromagnetic interaction is weak), so the magnetization saturates already above approximately 1 T [3,13]. Therefore, the demagnetizing field is not negligible even at weak external magnetic fields, and at the same time, it has a finite value (limited by the saturation magnetization), so it can be overcome by a strong external field. This corresponds to the disappearance of the seeming anisotropy above a moderate threshold field strength.

The demagnetizing magnetic flux density \mathbf{B}_d or, equivalently, the field strength \mathbf{H}_d , inside the sample with magnetization \mathbf{M} can be expressed as [17]

$$\mathbf{B}_d = \mu_0 \mathbf{H}_d = -\mu_0 \vec{N} \cdot \mathbf{M}. \quad (2)$$

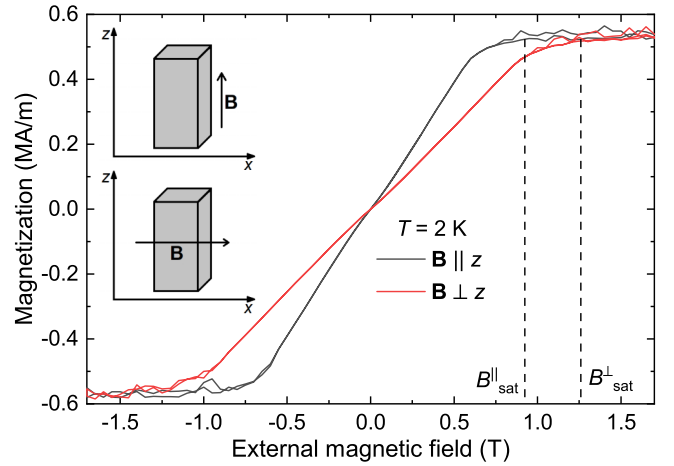


FIG. 3. Magnetization of the cuboid sample measured as a function of external magnetic field for both orientations ($\mathbf{B} \parallel z$ and $\mathbf{B} \perp z$) at $T = 2$ K. $B_{\text{sat}}^{\parallel}$, B_{sat}^{\perp} denote the values of the saturation external magnetic field for the corresponding orientations. Inset: Orientations of the sample with respect to the external magnetic field.

Here \vec{N} represents the *demagnetizing factor* which is a second-rank tensor determined by the shape of the magnetized body. Considering an ellipsoid whose principal axes coincide with the coordinate axes, only the diagonal elements $N_{xx} = N_x$, $N_{yy} = N_y$, $N_{zz} = N_z$ of the tensor \vec{N} are nonzero. For an elongated ellipsoid (prolate spheroid) with the long axis in the z direction, it holds that $N_x = N_y \approx \frac{1}{2}$ and $N_z \approx 0$. These demagnetizing factors can be used for the inherently isotropic (ceramic) cuboid EuTiO_3 sample (see inset of Fig. 3). Thus, if the external magnetic field \mathbf{B} is applied along the x or y axis, the demagnetizing magnetic flux density is equal to

$$B_d^x = -1/2\mu_0 M^x, \quad B_d^y = -1/2\mu_0 M^y. \quad (3)$$

By contrast, if the external magnetic field \mathbf{B} is applied along the z axis, the internal magnetic flux density is not affected by the demagnetizing field ($\mathbf{B}_d = 0$).

A flattened ellipsoid (oblate spheroid) with the short axis in the z direction is characterized by $N_x = N_y \approx 0$ and $N_z \approx 1$ [17]. A sample in the shape of a disk or plate can be thus approximated by an oblate spheroid. If \mathbf{B} is applied in the sample plane, the internal magnetic flux density is not affected ($B_d^x = B_d^y = 0$). By contrast, if \mathbf{B} is applied perpendicularly to the plate (along the z axis), the demagnetizing field reduces the internal magnetic flux density by

$$B_d^z = -\mu_0 M^z. \quad (4)$$

B. Magnetization studies

To verify our hypothesis that the observed anisotropy is caused by the demagnetizing field, we decided to compare the predictions of the demagnetizing field model with the experimental results. For a quantitative evaluation of the demagnetizing field, the magnetization of the cuboid sample was measured (Fig. 3). The external field \mathbf{B} was oriented either parallel with or perpendicular to the long edge of the cuboid (z axis). At first, the Néel temperature value $T_N = 4.9$ K was determined from the temperature dependence of the magnetic

susceptibility (see Fig. S2 in the Supplemental Material [16]). This value is slightly lower than the one reported earlier $T_N = 5.5$ K [1], probably due to different individual characteristics of each sample (e.g., single crystal versus ceramics, oxygen vacancy concentration, porosity, grain size, etc.) imposed by the fabrication process.

The magnetization measurements presented below confirm that a relatively weak external field is sufficient for saturating the magnetization. The saturation field along the long edge ($B_{\text{sat}}^{\parallel} \approx 0.9$ T) is about 0.3 T weaker than that perpendicular to the z axis (Fig. 3). When the value of saturated magnetization is taken as 0.5 MA/m, then the demagnetizing field calculation gives $B_d^x = 0.3$ T [according to Eq. (3)], which exactly corresponds to our experimental data. Note that in the magnetodielectric measurement (Fig. 2), $B_{\text{sat}}^{\parallel} - B_{\text{sat}}^{\perp} = 0.6$ T because the demagnetizing field should be, according to Eq. (4), twice larger in the disk-shaped sample than in the cuboid sample [Eq. (3)]. Thus, this comparison of the theory and the experiment rules out an intrinsic anisotropic magnetodielectric effect in EuTiO_3 ceramics. Note also that the values of saturation external magnetic field in the orientations without demagnetizing field are not the same in the magnetodielectric (Fig. 2) and magnetization (Fig. 3) data. This is, however, just due to different temperatures in both experiments (0.35 K and 2 K, respectively).

In the end of this section, we would like to add that the magnetodielectric effect was also investigated on several other samples with various thicknesses. However, the seemingly anisotropic effect was found to always be the same as the sample thickness was in every case much smaller than the sample plate diameter, so the demagnetizing field was always the same.

C. Infrared reflectivity and time-domain THz spectroscopic studies

The frequency-dependent complex refractive index $\hat{N}(\omega) = n(\omega) + ik(\omega)$ is equal to the product $\hat{N}^2 = \varepsilon\mu$ of dielectric permittivity $\varepsilon(\omega) = \varepsilon_1(\omega) + i\varepsilon_2(\omega)$ and complex magnetic permeability $\mu(\omega) = \mu_1(\omega) + i\mu_2(\omega)$ [18]. In the IR range, there is usually no magnetic excitation ($\mu = 1$), so $\hat{N}^2 = \varepsilon$. In these cases, it is possible to fit IR and THz reflectivity $R(\omega)$ using the formula

$$R(\omega) = \left| \frac{\sqrt{\varepsilon(\omega)} - 1}{\sqrt{\varepsilon(\omega)} + 1} \right|^2, \quad (5)$$

where the phonon contribution to ε can be expressed using the four-parameter oscillator model [19]:

$$\varepsilon(\omega) = \varepsilon_{\infty} \prod_{j=1}^n \frac{\omega_{\text{LO}_j}^2 - \omega^2 - i\gamma_{\text{LO}_j}\omega}{\omega_{\text{TO}_j}^2 - \omega^2 - i\gamma_{\text{TO}_j}\omega}. \quad (6)$$

Here ε_{∞} is the temperature-independent high-frequency permittivity owing to the electron transitions, ω_{TO_j} and γ_{TO_j} are the eigenfrequency and damping of the j th transverse optical phonon, ω_{LO_j} and γ_{LO_j} mark the eigenfrequency and damping of the j th longitudinal optical phonon.

In the present case of EuTiO_3 , as we show below, there is a weak contribution to $\mu(\omega)$ in the frequency range below 1 THz. Thus, Eqs. (5) and (6) remain valid for fitting the

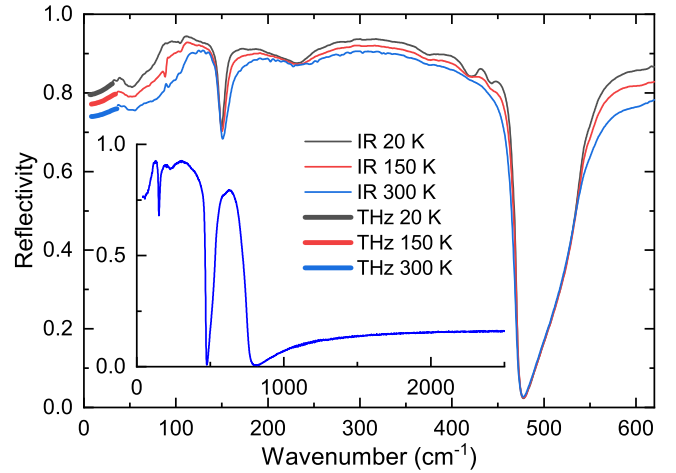


FIG. 4. Selected IR reflectivity spectra measured at different temperatures. The inset shows the complete room-temperature spectrum up to 2500 cm^{-1} . The reflectivity calculated from the measured THz spectra is shown by the thicker lines below 30 cm^{-1} .

IR spectra, providing a background phonon contribution for modeling the data in the THz range. Below 30 cm^{-1} , for a correct physical description of the optical properties, it is necessary to also take into account a magnon which shapes the permeability spectra.

The measured IR reflectivity spectra are depicted in Fig. 4. This data was slightly normalized to match the more reliable THz spectra to achieve mutual continuity. EuTiO_3 is a well-known incipient ferroelectric [1] whose dielectric permittivity increases on cooling due to a soft phonon [20]. The phonon softening (decrease in eigenfrequency on cooling) is clearly observable in Fig. 4 as a downshift of the low-frequency edge of the reflection band near 100 cm^{-1} . It is also manifested by the increasing reflectivity below approx. 140 cm^{-1} . Spectra fitting revealed that in the temperature interval 300–20 K, the phonon softens by about 20 cm^{-1} ; a similar effect was reported in Ref. [9]. We note also that an additional weak reflection band is observed near 40 cm^{-1} . Since the reflection band between 80 and 150 cm^{-1} consists of two modes, and because this doublet was previously explained by a tetragonal distortion of the antiferrodistortive phase [9], the activity of the additional mode can be explained only by a symmetry lower than tetragonal. Indications of such lower crystal symmetries in EuTiO_3 were observed in low-temperature birefringence and muon-spin-resonance studies by Bussmann-Holder *et al.* [6]; direct structural evidence is still missing, though. Considering the fact that the above-mentioned additional mode is also present at 300 K where the structure should be cubic, this mode is probably defect-induced.

Since, below T_N , the low-frequency permittivity increases with the external magnetic field, and because ε_1 is determined by the sum of phonon contributions, the increase in ε_1 with B should be seen also in the THz spectra. The measurements in the external magnetic field were carried out in the Voigt geometry. The external magnetic field was applied in the sample plane. Then, the demagnetizing field was zero. In view

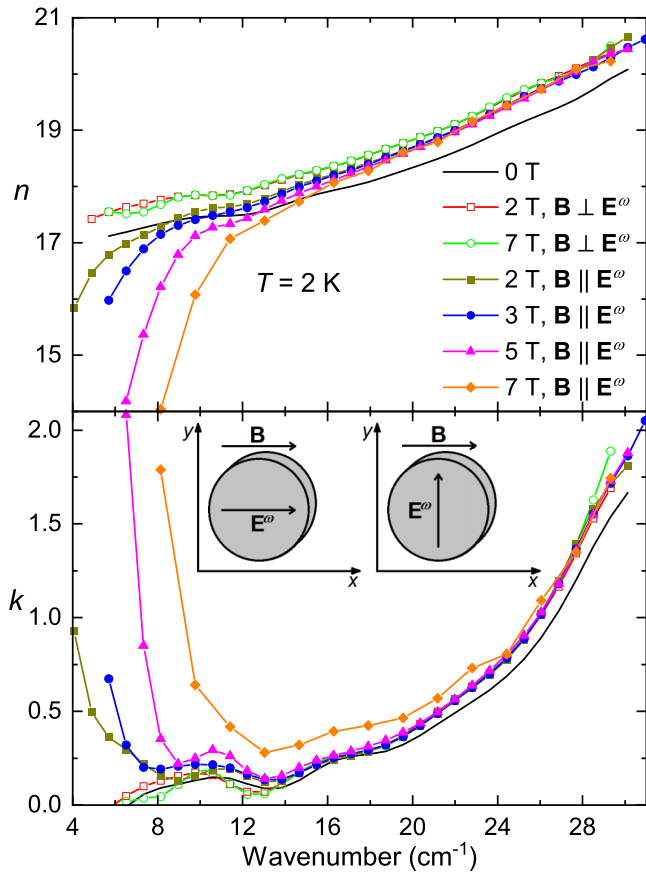


FIG. 5. Complex spectra of the THz refractive index $\hat{N} = n + ik$ at $T = 2$ K for selected external magnetic field values and the two orientations $\mathbf{B} \parallel \mathbf{E}^\omega$ and $\mathbf{B} \perp \mathbf{E}^\omega$. Inset: Orientations of vectors \mathbf{B} and \mathbf{E}^ω with respect to the sample.

of that, the spectra measured at $\mathbf{B} \parallel \mathbf{E}^\omega$ and $\mathbf{B} \perp \mathbf{E}^\omega$ could be expected to be the same.

This, however, was not confirmed by our observations (see Fig. 5). In the spectra for $\mathbf{B} \perp \mathbf{E}^\omega$, $n(\omega)$ slightly increases between 0 and 2 T, which is due to the rise in ϵ_1 with \mathbf{B} (as also seen in Fig. 2). At higher external magnetic fields, $n(\omega)$ remains unchanged due to the saturation of $\epsilon_1(B)$. The extinction coefficient $k(\omega)$ almost does not change with \mathbf{B} . Quite a different behavior is observed in the THz refractive index spectra for $\mathbf{B} \parallel \mathbf{E}^\omega$ (Fig. 5). Their high-frequency part rises between 0 and 2 T, and it saturates in higher fields as in the previous case. However, in the low-frequency interval, upon increasing \mathbf{B} , a decrease in $n(\omega)$ and an increase in $k(\omega)$ spectra are observed. This behavior is prominent mainly in stronger external magnetic fields, above approximately 1.5 T.

Since $\hat{N}^2 = \epsilon\mu$, the observed changes must be linked to variations in the magnetic permeability spectra. These can be explained by the presence of a magnon which, at low external magnetic fields, is located in the GHz frequency region [21,22], so it can be observed as the so-called ferromagnetic resonance. With increasing external magnetic field, its eigenfrequency is rising, so the magnon starts to influence the low-frequency THz spectra. The magnetic excitation is, however, present in the spectra only if $\mathbf{B} \parallel \mathbf{E}^\omega$, i.e., when the magnetic component of the THz radiation is oriented

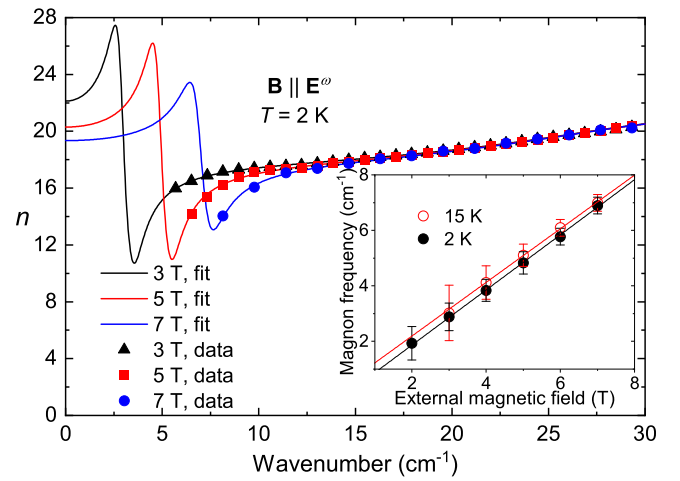


FIG. 6. Selected refractive index spectra of EuTiO_3 , measured at $T = 2$ K in the configuration $\mathbf{B} \parallel \mathbf{E}^\omega$. Symbols: Experimental results. Lines: Fits using Eq. (7) expressing a magnetic oscillator. Inset: External magnetic field dependencies of the magnetic excitation frequency $\omega_m(B)$ for $T = 2$ K and $T = 15$ K; symbols: values determined from the $\hat{N}(\omega)$ spectra fits; lines: linear fits. See text for more details.

perpendicular to the external static field, $\mathbf{B}^\omega \perp \mathbf{B}$. This observation supports the idea that the magnon is observed as the ferromagnetic resonance because its excitation in ceramics (where the magnetization is parallel with the external magnetic field \mathbf{B}) is determined by the nonzero value of the cross product $\mathbf{B} \times \mathbf{B}^\omega$ [23]. In the case of $\mathbf{B} \parallel \mathbf{B}^\omega$, the cross product is zero, therefore the ferromagnetic resonance cannot be excited and it does not contribute to the $\hat{N}(\omega)$ spectra.

The magnon response can be fitted using the harmonic oscillator formula [24],

$$\mu(\omega) = \mu_\infty + \frac{\Delta\mu\omega_m^2}{\omega_m^2 - \omega^2 - i\gamma_m\omega}, \quad (7)$$

where μ_∞ is the temperature-independent high-frequency permeability (in our case, equal to 1), $\Delta\mu = \mu(0) - \mu_\infty$ denotes the magnon contribution to the static permeability, ω_m represents the magnon frequency and γ_m its damping.

Fits of selected THz spectra measured at $T = 2$ K in the configuration $\mathbf{B} \parallel \mathbf{E}^\omega$ are displayed in Fig. 6. In addition to the magnon term described by Eq. (7), the permittivity model due to the phonons describing the IR spectra at 20 K [Eq. (6)] was used (for complex permittivity, complex permeability and real conductivity spectra obtained from this fitting model, please also see Figs. S3 and S5 in the Supplemental Material [16]). There is a good correspondence between the measured data and the fitting model. The inset of Fig. 6 shows the evolution of the magnon frequency values with external magnetic field, $\omega_m(B)$. The magnon frequency clearly follows a linear dependence on the external magnetic field. Interestingly, the shapes of the complex $\hat{N}(\omega)$ spectra reveal the magnon presence also at 15 K, as much as 10 K above T_N . The existence of the ferromagnetic resonance in the paramagnetic phase was reported earlier [22]. It is a consequence of the external magnetic field, which stabilizes the ferromagneticlike structure well above T_N .

We have performed linear fits of the magnon frequency values by the formula $\omega_m(B) = \gamma \cdot B + \omega(0)$. Here γ represents the gyromagnetic ratio [23] $\gamma = g\mu_B/h$ defined using the Planck's constant h , Bohr's magneton μ_B , and the g factor whose nonrelativistic value for spin magnetic system equals 2. According to the Hund's rules, a magnetic lattice composed of Eu^{2+} ions should act as such a spin system, therefore a value of $\gamma = 0.93 \text{ cm}^{-1} \text{ T}^{-1}$ is expected. The performed fit yields the values $\gamma = (0.99 \pm 0.02) \text{ cm}^{-1} \text{ T}^{-1}$, $\omega(0) = (-0.1 \pm 0.1) \text{ cm}^{-1}$ for the temperature $T = 2 \text{ K}$ and $\gamma = (0.97 \pm 0.02) \text{ cm}^{-1} \text{ T}^{-1}$, $\omega(0) = (0.3 \pm 0.1) \text{ cm}^{-1}$ for the temperature $T = 15 \text{ K}$. These experimentally obtained values of γ agree very well with the expected spin magnetism of Eu^{2+} ions. Within the fitting error, the fits for both 2 K and 15 K exhibit the same slope γ , and they differ a little in their intercepts $\omega(0)$. This can probably be attributed to the absence of reliable data below 5 cm^{-1} and to the absence of magnon spectral signatures for the external magnetic fields below 2 T. Thus, the overall uncertainties in the parameters γ and $\omega(0)$ may be higher than the error values given above, and we cannot effectively compare the obtained magnon frequencies in weak external magnetic fields with those reported previously [21,22].

Earlier, the group of Bussmann-Holder discovered a magnetic-field-dependent specific heat anomaly near the temperature of the antiferrodistortive phase transition [25]. At the same temperature, a magnetic susceptibility anomaly was observed [6]. These facts together with results of magnetic-field-dependent muon spin rotation studies [26] suggest a dynamically fluctuating short-range magnetic order in the paramagnetic phase of EuTiO_3 . For that reason, Bussmann-Holder *et al.* hypothesized an opticlike paramagnon branch above T_N whose coupling with the soft optical phonon branch was used for explanation of the soft phonon saturation observed on cooling [27]. In that case, the paramagnon should exhibit an eigenfrequency near 70 cm^{-1} , but no such paramagnon is visible in our data. Nevertheless, there is a mode visible near 40 cm^{-1} (see Fig. 4) which cannot be explained as a phonon in the tetragonal phase. However, its assignment to the paramagnon is also unlikely because it is temperature independent and the shape of the appropriate reflection band does not resemble the one typical of magnetic excitations [28]. Therefore, the explanation of this mode will require further optical studies.

Based on the fits of the THz and IR spectra, it is possible to compare the magnetic-field-dependent phonon permittivities for $\mathbf{B} \parallel \mathbf{E}^\omega$ and $\mathbf{B} \perp \mathbf{E}^\omega$. This is shown in Fig. 7, which presents the quasistatic permittivity $\varepsilon_1(0)$ (obtained by extrapolating the THz data fits to zero frequency) as a function of the external magnetic field. Within the whole interval of B , at 2 K, there is no difference between the curves for the two orientations, $\mathbf{B} \parallel \mathbf{E}^\omega$ and $\mathbf{B} \perp \mathbf{E}^\omega$. Note that the demagnetizing field is zero in both configurations. The rise in $\varepsilon_1(0)$ for $B \leq 2 \text{ T}$ is a consequence of the fact that the frequency of the soft phonon near 90 cm^{-1} decreases by 2 cm^{-1} within this interval (see the parameters listed in Table II in the Supplemental Material [16]). Note that this decrease is quantitatively similar to the one observed in a EuTiO_3 film (grown on a LSAT substrate) subjected to a compressive strain of 0.9% [29].

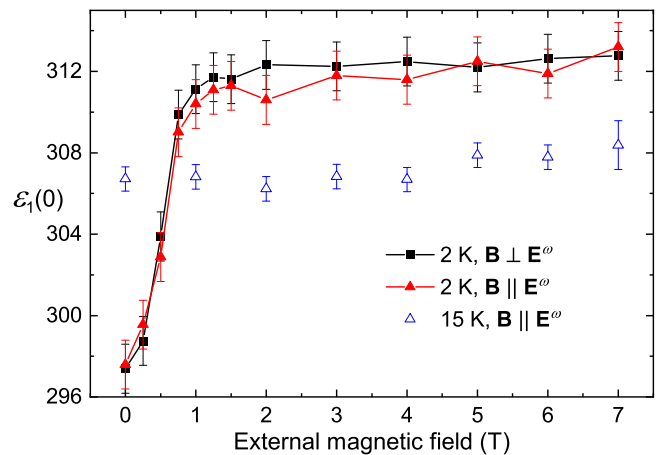


FIG. 7. Quasistatic permittivity $\varepsilon_1(0)$ as a function of the external magnetic field. Symbols: Data obtained from fits of the THz spectra collected for temperatures 2 K and 15 K at both field orientations, $\mathbf{B} \perp \mathbf{E}^\omega$ and $\mathbf{B} \parallel \mathbf{E}^\omega$. The lines are guides for the eye.

The shapes of the $\varepsilon_1(0)(B)$ curves shown in Fig. 7 correspond very well to the observed low-frequency magnetodielectric effect (see Fig. 2, the data for $\mathbf{B} \perp \mathbf{E}^\omega$ without the demagnetizing field influence). This confirms the validity of the approach used for spectra fitting. The values of low-frequency ε_1 are higher than those obtained from the THz and IR fits; this can be explained by an additional weak term located in the microwave region, leading to a small dielectric dispersion and enhancing the low-frequency permittivity ε_1 . Note that the value of $\varepsilon_1(0)$ at 15 K is not influenced by the external magnetic field (see Fig. 7). This is more or less expected because the material is in the paramagnetic state where the spin-phonon coupling plays no role. At 15 K, small changes in ε_1 at low frequencies upon applying external magnetic fields were observed (see Fig. 1). However, this is probably due to changes in the microwave and low-frequency dispersion with external magnetic field, originating in the presence of defects and the related small Maxwell-Wagner polarization.

IV. CONCLUSION

Experimental investigations of the complex THz refractive index of EuTiO_3 ceramics revealed an anisotropy with respect to the mutual orientation between the static external magnetic field \mathbf{B} and the polarization of the THz radiation magnetic component \mathbf{B}^ω . The anisotropy was attributed to a ferromagnetic resonance which is excited only in the configuration $\mathbf{B} \perp \mathbf{B}^\omega$ or, equivalently, if the cross product $\mathbf{B} \times \mathbf{B}^\omega$ is nonzero. It was also shown that the ferromagnetic resonance frequency is linearly proportional to the external static magnetic field, thus moving from the microwave to the sub-THz region. This holds true also at $T = 15 \text{ K}$, nearly 10 K above T_N . The proportionality constants (gyromagnetic ratios) $\gamma = (0.99 \pm 0.02) \text{ cm}^{-1} \text{ T}^{-1}$ for the temperature $T = 2 \text{ K}$ and $\gamma = (0.97 \pm 0.02) \text{ cm}^{-1} \text{ T}^{-1}$ for the temperature $T = 15 \text{ K}$ agree very well with the expected value $\gamma = 0.93 \text{ cm}^{-1} \text{ T}^{-1}$ describing the dynamics of purely spin-based magnetic moments attached to Eu^{2+} ions.

We presented observations of an “anisotropy” of permittivity in the low-frequency region at an applied external static magnetic field of up to 2 T. This effect was explained by the presence of the demagnetizing field due to the shapes of the samples. The experimental results were compared with simple calculations of the demagnetizing field. These were based on the measured value of saturation magnetization in the EuTiO_3 ceramics and on an approximation of very oblate and prolate ellipsoidal specimens representing our disk-shaped and cuboid samples, respectively. The comparison has yielded a quantitative match between the theoretical and experimental results.

The important role of the demagnetizing field in the EuTiO_3 ceramics is due to the large value of saturation magnetization. The latter is caused by high magnetic moments originating from spins of seven valence electrons carried by Eu^{2+} ions and also by the fact that these ions are bound by a rather weak exchange interaction; consequently, the Eu spins are easily orientable. The seeming anisotropy of the low-frequency permittivity vanishes at external magnetic fields stronger than ≈ 2 T, as the demagnetizing field is overcome by the external magnetic field; in that situation, the sample magnetization is already saturated in all configurations. Our observations and the proposed explanation of the seeming magnetodielectric effect aim to draw attention to the demagnetizing field issue. There are many articles about magnetodielectric studies on ceramics, but, as a rule, they do not take into account the demagnetizing factors for determining the magnetodielectric coupling at low magnetic fields [30,31].

We have demonstrated that when one uses disk-shaped or rectangular flat samples, for observing the highest magnetodielectric coupling effect, the external magnetic field should be applied in the sample plane. It should also be noted that the sample shape and related demagnetizing field can have influence on the magnon frequency in ferrimagnetic or ferromagnetic single crystals even in the zero external magnetic field. Therefore, the demagnetizing field should be taken into account in the future studies of the magnetoelectric coupling in various multiferroics.

ACKNOWLEDGMENTS

We are grateful to Jakub Vít for a critical reading of the paper and to Oleg Heczko for a helpful discussion on the demagnetizing field and its relation to the observed seeming anisotropy. This work was supported by the Czech Science Foundation (Project No. 18-09265S), by the Operational Programme Research, Development and Education (financed by European Structural and Investment Funds and by the Czech Ministry of Education, Youth and Sports), by the project SOLID21 (Project No. CZ.02.1.01/0.0/0.0/16_019/0000760), by the program of Czech Research Infrastructures (Project No. LM2018096), and by the Grant Agency of the Czech Technical University in Prague (Project No. SGS16/244/OHK4/3T/14). We also acknowledge the support of Brno University of Technology (Grant No. FSI-S-20-6292) and a financial support of the MEYS of the Czech Republic under Project No. CEITEC 2020 (LQ1601).

-
- [1] T. Katsufuji and H. Takagi, *Phys. Rev. B* **64**, 054415 (2001).
 - [2] H. Wu, Q. Jiang, and W. Shen, *Phys. Lett. A* **330**, 358 (2004).
 - [3] V. V. Shvartsman, P. Borisov, W. Kleemann, S. Kamba, and T. Katsufuji, *Phys. Rev. B* **81**, 064426 (2010).
 - [4] J. H. Lee, L. Fang, E. Vlahos, X. Ke, Y. W. Jung, L. F. Kourkoutis, J.-W. Kim, P. J. Ryan, T. Heeg, M. Roeckerath *et al.*, *Nature* **466**, 954 (2010).
 - [5] A. Bussmann-Holder and J. Köhler, *J. Phys. Chem. Sol.* **84**, 2 (2015).
 - [6] A. Bussmann-Holder, J. Köhler, K. Roleder, Z. Guguchia, and H. Keller, *Thin Solid Films* **643**, 3 (2017).
 - [7] J. Brous, I. Fankuchen, and E. Banks, *Acta Cryst.* **6**, 67 (1953).
 - [8] A. Bussmann-Holder, J. Köhler, R. K. Kremer, and J. M. Law, *Phys. Rev. B* **83**, 212102 (2011).
 - [9] V. Goian, S. Kamba, O. Pacherová, J. Drahoš, L. Palatinus, M. Dušek, J. Rohlíček, M. Savinov, F. Laufek, W. Schranz, A. Fuith, M. Kachlik, K. Maca, A. Shkabko, L. Sagarna, A. Weidenkaff, and A. A. Belik, *Phys. Rev. B* **86**, 054112 (2012).
 - [10] J. Köhler, R. Dinnebier, and A. Bussmann-Holder, *Phase Trans.* **85**, 949 (2012).
 - [11] V. Scagnoli, M. Allieta, H. Walker, M. Scavini, T. Katsufuji, L. Sagarna, O. Zaharko, and C. Mazzoli, *Phys. Rev. B* **86**, 094432 (2012).
 - [12] T. McGuire, M. Shafer, R. Joenk, H. Alperin, and S. Pickart, *J. Appl. Phys.* **37**, 981 (1966).
 - [13] P. G. Reuvekamp, R. K. Kremer, J. Köhler, and A. Bussmann-Holder, *Phys. Rev. B* **90**, 094420 (2014).
 - [14] M. Kachlík, K. Maca, V. Goian, and S. Kamba, *Mater. Lett.* **74**, 16 (2012).
 - [15] V. Valvoda and M. Järvinen, *Powder Diff.* **5**, 200 (1990).
 - [16] See Supplemental Material at <http://link.aps.org/supplemental/10.1103/PhysRevB.102.144402> for phonon and magnon parameters, image of sample surface, magnetic field dependence of complex permittivity, real part of optical conductivity and magnetic permeability together with temperature dependence of magnetic susceptibility.
 - [17] S. Chikazumi and C. D. Graham, *Physics of Ferromagnetism*, 2nd ed. (Oxford University Press, New York, USA, 2009), Vol. 94.
 - [18] M. Dressel and G. Grüner, *Electrodynamics of Solids: Optical Properties of Electrons in Matter* (Cambridge University Press, Cambridge, 2002), Chap. 2, pp. 11–42.
 - [19] R. Lowndes, *Phys. Rev. B* **1**, 2754 (1970).
 - [20] S. Kamba, D. Nuzhnyy, P. Vaněk, M. Savinov, K. Knížek, Z. Shen, E. Šantavá, K. Maca, M. Sadowski, and J. Petzelt, *Europhys. Lett.* **80**, 27002 (2007).
 - [21] J. L. M. van Mechelen, D. van der Marel, I. Crassee, and T. Kolodiaznyy, *Phys. Rev. Lett.* **106**, 217601 (2011).
 - [22] V. Laguta, S. Kamba, M. Maryško, B. Andrzejewski, M. Kachlík, K. Maca, J. Lee, and D. Schlom, *J. Phys.: Condens. Matter* **29**, 105401 (2017).
 - [23] C. Kittel, *Introduction to Solid State Physics* (John Wiley & Sons, Inc, New Jersey, 2005), Chaps. 12 and 13, pp. 330–392.

- [24] A. Balbashov, G. Kozlov, A. Mukhin, and A. Prokhorov, *High Frequency Processes in Magnetic Materials* (World Scientific Pub. Co. Inc, Singapore, 1995), Chap. 2, pp. 56–98.
- [25] Z. Guguchia, H. Keller, J. Köhler, and A. Bussmann-Holder, *J. Phys.: Condens. Matter* **24**, 492201 (2012).
- [26] Z. Guguchia, H. Keller, R. K. Kremer, J. Köhler, H. Luetkens, T. Goko, A. Amato, and A. Bussmann-Holder, *Phys. Rev. B* **90**, 064413 (2014).
- [27] A. Bussmann-Holder, Z. Guguchia, J. Köhler, H. Keller, A. Shengelaya, and A. Bishop, *New J. Phys.* **14**, 093013 (2012).
- [28] A. Mukhin, A. Y. Pronin, A. Prokhorov, G. Kozlov, V. Zelezny, and J. Petzelt, *Phys. Lett. A* **153**, 499 (1991).
- [29] S. Kamba, V. Goian, M. Orlita, D. Nuzhnyy, J. H. Lee, D. G. Schlom, K. Z. Rushchanskii, M. Ležaić, T. Birol, C. J. Fennie, P. Gemeiner, B. Dkhil, V. Bovtun, M. Kempa, J. Hlinka, and J. Petzelt, *Phys. Rev. B* **85**, 094435 (2012).
- [30] S. K. Upadhyay, P. L. Paulose, and E. V. Sampathkumaran, *Phys. Rev. B* **96**, 014418 (2017).
- [31] X. Shen, L. Zhou, X. Ye, Z. Liu, G. Liu, S. Qin, J. Guo, L. Gao, Y. Chai, and Y. Long, *Appl. Phys. Lett.* **116**, 052901 (2020).